SXDF-ALMA 2 arcmin² deep survey: Resolving and characterizing the infrared extragalactic background light down to 0.5 mJy

Yuki YAMAGUCHI,[1,*] Yoichi TAMURA,[1] Kotaro KOHNO,[1,2] Itziar ARETXAGA,[3] James S. DUNLOP,[4] Bunyo HATSUKADE,[5] David HUGHES,[3] Soh IKARASHI,[6] Shun ISHII,[1] Rob J. IVISON,[4,7] Takuma IZUMI,[1] Ryohei KAWABE,[5,8,9] Tadayuki KODAMA,[5,9] Minju LEE,[5,8] Ryu MAKIYA,[10,11] Yuichi MATSUDA,[5,9] Kouichiro NAKANISHI,[5,9] Kouji OHTA,[12] Wiphu RUJOPAKARN,[10,13] Ken-ichi TADAKI,[14] Hideki UMEHATA,[1] Wei-Hao WANG,[15] Grant W. WILSON,[16] Kiyoto YABE,[10] and Min S. YUN[16]

[1]Institute of Astronomy, The University of Tokyo, 2-21-1 Osawa, Mitaka, Tokyo 181-0015, Japan
[2]Research Center for the Early Universe, The University of Tokyo, 7-3-1 Hongo, Bunkyo-ku, Tokyo 113-0033, Japan
[3]Instituto Nacional de Astrofísica, Óptica y Electrónica, Tonantzintla, Luis Enrique Erro 1, Santa María Tonantzintla, Puebla, México
[4]Institute for Astronomy, University of Edinburgh, Royal Observatory, Blackford Hill, Edinburgh, EH9 3HJ, UK
[5]National Astronomical Observatory of Japan, 2-21-1 Osawa, Mitaka, Tokyo 181-8588, Japan
[6]Kapteyn Astronomical Institute, University of Groningen, P.O. Box 800, 9700AV Groningen, The Netherlands
[7]European Southern Observatory, Karl-Schwarzschild-Str. 2, D-85748 Garching, Germany
[8]Department of Astronomy, School of Science, The University of Tokyo, 7-3-1 Hongo, Bunkyo-ku, Tokyo 113-0033, Japan
[9]The Graduate University for Advanced Studies (SOKENDAI), 2-21-1 Osawa, Mitaka, Tokyo 181-8588, Japan
[10]Kavli Institute for the Physics and Mathematics of the Universe (Kavli IPMU, WPI), Todai Institutes for Advanced Study, The University of Tokyo, 5-1-5 Kashiwanoha, Kashiwa, Chiba 277-8583, Japan
[11]Max-Planck-Institut für Astrophysik, Karl-Schwarzschild Str. 1, D-85741 Garching, Germany
[12]Department of Astronomy, Kyoto University, Kitashirakawa-oiwake-cho, Sakyo-ku, Kyoto, Kyoto 606-8502, Japan
[13]Department of Physics, Faculty of Science, Chulalongkorn University, 254 Phayathai Road, Pathumwan, Bangkok 10330, Thailand
[14]Max-Planck-Institut für Extraterrestrische Physik (MPE), Giessenbachstr., D-85748 Garching, Germany
[15]Institute of Astronomy and Astrophysics, Academia Sinica, Taipei 10617, Taiwan
[16]Department of Astronomy, University of Massachusetts, 710 North Pleasant St., Amherst, MA 01003, USA

*E-mail: yyamaguchi@ioa.s.u-tokyo.ac.jp

Abstract

We present a multiwavelength analysis of five submillimeter sources ($S_{1.1mm} = 0.54$–2.02 mJy) that were detected during our 1.1 mm deep continuum survey in the Subaru/XMM-Newton Deep Survey Field (SXDF)-UDS-CANDELS field (2 arcmin^2, $1\sigma = 0.055$ mJy beam^{-1}) using the Atacama Large Millimeter/submillimeter Array (ALMA). The two brightest sources correspond to a known single-dish (AzTEC) selected bright submillimeter galaxy (SMG), whereas the remaining three are faint SMGs newly uncovered by ALMA. If we exclude the two brightest sources, the contribution of the ALMA-detected faint SMGs to the infrared extragalactic background light is estimated to be $\sim 4.1^{+5.4}_{-3.0}$ Jy deg^{-2}, which corresponds to $\sim 16^{+22}_{-12}\%$ of the infrared extragalactic background light. This suggests that their contribution to the infrared extragalactic background light is as large as that of bright SMGs. We identified multiwavelength counterparts of the five ALMA sources. One of the sources (SXDF-ALMA3) is extremely faint in the optical to near-infrared region despite its infrared luminosity ($L_{IR} \simeq 1 \times 10^{12} L_{\odot}$ or SFR $\simeq 100 M_{\odot}$ yr^{-1}). By fitting the spectral energy distributions at the optical-to-near-infrared wavelengths of the remaining four ALMA sources, we obtained the photometric redshifts (z_{photo}) and stellar masses (M_*): $z_{photo} \simeq 1.3$–2.5, $M_* \simeq (3.5$–$9.5) \times 10^{10} M_{\odot}$. We also derived their star formation rates (SFRs) and specific SFRs as $\simeq 30$–$200 M_{\odot}$ yr^{-1} and $\simeq 0.8$–2 Gyr^{-1}, respectively. These values imply that they are main sequence star-forming galaxies.

Key words: galaxies: high-redshift — galaxies: star formation — submillimeter: galaxies

1 Introduction

Determining the contributors of dust-obscured galaxies to the cosmic star formation rate density (cosmic SFRD) is a major goal of deep surveys at far-infrared, millimeter, submillimeter, and radio wavelengths. In fact, deep surveys using the Infrared Space Observatory (ISO), AKARI, and the Herschel Space Observatory (Herschel) have revealed that dusty star-forming galaxies largely dominate the cosmic SFRD up to the redshift $z \approx 1$–3 (e.g., Takeuchi et al. 2005; Goto et al. 2011; Burgarella et al. 2013).

Over the past decade, a series of wide-area surveys performed at millimeter/submillimeter wavelengths using single-dish telescopes has revealed many bright submillimeter galaxies (SMGs; e.g., Smail et al. 1997; Hughes et al. 1998; Barger et al. 1998; Blain et al. 2002; Greve et al. 2004; Weiß et al. 2009; Scott et al. 2010; Hatsukade et al. 2011; Casey et al. 2013; Umehata et al. 2014, and references therein) with observed flux densities larger than a few mJy at millimeter/submillimeter wavelengths. They have large total infrared (IR; rest-frame 8–1000 μm) luminosities ($L_{IR} \sim 10^{12-13} L_{\odot}$) powered by dust-obscured star formation (e.g., Alexander et al. 2005; Laird et al. 2010), and their redshift distribution peaks are at $z \approx 2.2$–2.5 (e.g., Chapman et al. 2005; Simpson et al. 2014). Their extreme star formation rates (SFRs $\gtrsim$ a few 100–1000 $M_{\odot}$ yr^{-1}) make them non-negligible contributors to cosmic star formation (e.g., Hughes et al. 1998;

Casey et al. 2013; Wardlow et al. 2011; Swinbank et al. 2014). However, the contribution of SMGs detected by single-dish surveys to the infrared extragalactic background light, which is believed to be the integrated infrared emissions from all extragalactic sources along the line of sight, is 20%–40% at 850 μm (e.g., Eales et al. 1999; Coppin et al. 2006; Weiß et al. 2009) and 10%–20% at 1.1 mm (e.g., Hatsukade et al. 2011; Scott et al. 2012). Thus, the bulk of infrared extragalactic background light remains unresolved with single-dish telescopes.

By using stacking analysis of K-selected galaxies, Greve et al. (2010) found that these galaxies contribute by $\simeq 16.5\%$ to the infrared extragalactic background light at 870 μm, although individual source properties remained unexplored in this stacking analysis.

The advent of the Atacama Large Millimeter/submillimeter Array (ALMA), which offers high sensitivity and angular resolution capabilities, has allowed a fainter population of SMGs to be unveiled below the confusion limit of single-dish telescopes. Here, we refer to the fainter population of SMGs with flux densities of ~ 0.1–1 mJy at 1.1–1.3 mm as "faint SMGs." Their estimated contributions to the infrared extragalactic background light are $\simeq 50\%$–80% (Hatsukade et al. 2013; Ono et al. 2014; Oteo et al. 2016). Deeper number counts down to ~ 0.02 mJy have recently obtained by Carniani et al. (2015) and Fujimoto et al. (2016), who claimed that $\sim 100\%$ of the infrared extragalactic background

light is resolved at 1.2–1.3 mm. These results suggest that faint SMGs can play an important role in the cosmic star formation activities at high redshifts. However, their contributions to the cosmic SFRD are still unknown because of the lack of redshift information.

Single-dish telescopes have been used in attempts to detect faint SMGs with the aid of gravitational magnification by lensing clusters. For example, Knudsen, van der Werf, and Kneib (2008) constrained the faint end ($S_{850\mu m} \simeq 0.1$ mJy) of the 850 μm number counts by using cluster magnification. Chen et al. (2014) performed follow-up observations of these lensed faint SMGs by using the submillimeter array (SMA: Moran 1998) and implied that there are many faint SMGs that are faint at optical/near-infrared wavelengths and have been missed in deep optical/near-infrared surveys. In lens surveys, however, the effective sensitivity comes at the cost of a reduced survey volume; the effective (source-plane) area within sufficient magnification for faint SMG detection is only ~ 0.1 arcmin^2 for a typical rich cluster (Knudsen et al. 2008).[1] This also increases the cosmic variance uncertainty (e.g., Robertson et al. 2014). Therefore, it is still necessary to obtain wide (>1 arcmin^2) and deep ($1\sigma \lesssim 0.1$ mJy) blank/unlensed field surveys at a higher angular resolution to gain a better understanding of faint SMGs and their true contributions to the cosmic SFRD.

Another key issue in understanding galaxy evolution is the star formation properties of galaxies. Star-forming galaxies have a correlation between their stellar masses and SFRs, which is defined as a main sequence (e.g., Daddi et al. 2007; Rodighiero et al. 2011, 2014; Schreiber et al. 2015). Main sequence star-forming galaxies are "normal" star-forming galaxies selected by optical/near-infrared colors [e.g., *BzK* galaxies, typical specific SFRs (sSFRs) ~ 1 Gyr^{-1} at $z \sim 1.4$–2.5; Rodighiero et al. 2011]. However, outliers of the correlation exist with higher sSFRs than those of main sequence star formation galaxies (sSFRs $\gtrsim 10^1$–10^2 Gyr^{-1} at $z \sim 1.4$–2.5: Rodighiero et al. 2011). These outliers are often referred to as starburst galaxies. Many bright SMGs are classified as starburst galaxies or the high-mass end of main sequence galaxies (e.g., Takagi et al. 2008; Michałowski et al. 2012, 2014; Koprowski et al. 2014; da Cunha et al. 2015). However, it is not understood whether faint SMGs are on or above the main sequence because the stellar masses of these faint SMGs have not yet been measured. Understanding the star-forming properties of faint SMGs is also helpful in unveiling the evolution of the cosmic SFRD because they are thought to be the main contributor to the infrared extragalactic background light (e.g., Carniani et al. 2015; Fujimoto et al. 2016).

In this paper, we present spectral energy distributions (SEDs) for optical-to-radio counterparts to five sub-millimeter sources that were detected in our 2 arcmin^2 1.1 mm deep survey of the Subaru/XMM-Newton Deep Survey Field (SXDF: Furusawa et al. 2008) using ALMA (Project ID: 2012.1.00756.S, PI: K. Kohno) to understand their contribution to the infrared extragalactic background light and cosmic SFRD. We also discuss their multiwavelength properties. Our survey field was also covered by the UKIRT Infrared Deep Sky Survey Ultra-Deep Survey (UDS: Lawrence et al. 2007) and Cosmic Assembly Near-infrared Deep Extragalactic Legacy Survey (CANDELS: Grogin et al. 2011; Koekemoer et al. 2011).

This paper is structured as follows. Section 2 presents the ALMA observations and multiwavelength data used in this study. Section 3 presents the results of the multiwavelength counterpart identification of the ALMA sources. Section 4 derives the photometric redshift, stellar mass (M_*), SFRs, and sSFRs and presents the optical-to-radio SEDs. Sections 5 and 6 are devoted to the discussion and summary, respectively. Throughout this paper, we assume a Λ cold dark matter cosmology with $\Omega_M = 0.3$, $\Omega_\Lambda = 0.7$, and $H_0 = 70$ km s^{-1} Mpc^{-1}. All magnitudes are given according to the AB system.

2 Multiwavelength images

2.1 ALMA observations and source identifications

Here, we briefly summarize the ALMA data: their details will be given in a subsequent paper (K. Kohno et al. in preparation; see also Tadaki et al. 2015; Kohno et al. 2016; Hatsukade et al. 2016). The ALMA observations were carried out on 2014 July 17 and 18 (Cycle 1). The 2 arcmin^2 map of the SXDF-UDS-CANDELS field was obtained at 274 GHz (or 1.1 mm; Band 6). The region is centered at $(\alpha, \delta)_{\rm J2000.0} = (02^{\rm h}17^{\rm m}41\overset{\rm s}{.}31, -05°13'28\overset{''}{.}9)$ and is covered by 19 pointings of ALMA. For the observations, 30–32 antennas were employed, and the array was close to the C32-4 configuration, which has minimum and maximum baselines of 20 and 650 m, respectively (the synthesized beam is $0\overset{''}{.}53 \times 0\overset{''}{.}41$ with the position angle of 64° in the naturally weighted map). We performed our observations under good conditions, where the precipitable water vapor was in the range of 0.42–0.55 mm. The phase and bandpass were calibrated with J0215−0222 and J0241−0815, respectively. The flux was calibrated with J2258−279 and J0238+166. The absolute calibration accuracy for Cycle 1 is 10% for Band 6 (ALMA Cycle 1 Technical Handbook). The data were processed with the Common Astronomy Software Application (CASA: McMullin et al. 2007). The

---

[1] Fujimoto et al. (2016) also used gravitational magnification from lensing clusters, and their survey area was ~ 0.5 arcmin^2 (source-plane).

Table 1. Multiwavelength photometry of our ALMA sources and their derived properties.*

		SXDF-ALMA1	SXDF-ALMA2	SXDF-ALMA3	SXDF-ALMA4	SXDF-ALMA5
$RA_{1.1mm}$[†]	(J2000.0)	$02^h17^m40^s.52$	$02^h17^m41^s.12$	$02^h17^m43^s.64$	$02^h17^m42^s.33$	$02^h17^m41^s.23$
$Dec_{1.1mm}$[†]	(J2000.0)	$-05°13'10''.64$	$-05°13'15''.19$	$-05°14'23''.81$	$-05°14'05''.09$	$-05°14'02''.73$
$S_{1.1mm;peak}$[‡]	[mJy/beam]	1.69 ± 0.06	0.92 ± 0.07	0.84 ± 0.09	0.36 ± 0.05	0.28 ± 0.05
$S_{1.1mm;total}$[§]	[mJy]	2.02 ± 0.12	1.38 ± 0.14	1.16 ± 0.19	0.54 ± 0.12	0.56 ± 0.14
$R.A._{F160W}$[‖]	(J2000.0)	$02^h17^m40^s.55$	$02^h17^m41^s.12$	—	$02^h17^m42^s.34$	$02^h17^m41^s.22$
$Dec._{F160W}$[‖]	(J2000.0)	$-05°13'10''.67$	$-05°13'14''.98$	—	$-05°14'05''.16$	$-05°14'02''.77$
Subaru/Suprime-Cam B	[mag]	>27.90	26.16 ± 0.07	—	27.07 ± 0.16	26.84 ± 0.13
Subaru/Suprime-Cam V	[mag]	>27.42	25.83 ± 0.08	—	26.98 ± 0.24	26.92 ± 0.22
Subaru/Suprime-Cam R_C	[mag]	>27.24	25.65 ± 0.08	—	25.96 ± 0.11	26.02 ± 0.11
Subaru/Suprime-Cam i'	[mag]	>27.11	25.62 ± 0.09	—	25.32 ± 0.07	25.45 ± 0.08
Subaru/Suprime-Cam z'	[mag]	>26.04	25.27 ± 0.18	—	24.24 ± 0.07	24.71 ± 0.11
HST/ACS $F606W$	[mag]	>25.93	25.25 ± 0.19	>25.93	25.63 ± 0.27	26.83 ± 0.84
HST/ACS $F814W$	[mag]	>25.84	25.38 ± 0.24	>25.84	24.65 ± 0.12	25.13 ± 0.19
HST/WFC3 $F125W$	[mag]	25.48 ± 0.30	24.28 ± 0.10	>25.66	22.98 ± 0.03	23.23 ± 0.04
HST/WFC3 $F160W$	[mag]	24.50 ± 0.12	23.58 ± 0.05	25.30 ± 0.25	22.40 ± 0.02	22.63 ± 0.02
VLT/HAWK-I Y	[mag]	>25.97	24.74 ± 0.12	>25.97	23.57 ± 0.04	23.82 ± 0.05
VLT/HAWK-I K_s	[mag]	23.42 ± 0.09	22.75 ± 0.05	24.69 ± 0.29	21.72 ± 0.02	21.92 ± 0.02
Spitzer/IRAC 3.6 μm	[mag]	22.08 ± 0.02	21.65 ± 0.02	24.08 ± 0.14	21.06 ± 0.01	21.04 ± 0.01
Spitzer/IRAC 4.5 μm	[mag]	21.57 ± 0.02	21.17 ± 0.02	23.59 ± 0.11	20.96 ± 0.01	20.74 ± 0.01
Spitzer/IRAC 5.8 μm	[mag]	21.51 ± 0.17	20.78 ± 0.24	>22.17	21.49 ± 0.10	20.93 ± 0.12
Spitzer/IRAC 8.0 μm	[mag]	21.12 ± 0.16	20.78 ± 0.12	>21.71	21.54 ± 0.24	21.03 ± 0.17
Spitzer/MIPS 24 μm	[mag]	18.66 ± 0.12	18.82 ± 0.13	>19.9	>19.9	19.53 ± 0.26
Herschel/PACS 100 μm	[mJy]	<6.72	<6.72	<6.72	<6.72	<6.72
Herschel/PACS 160 μm	[mJy]	<12.8	<12.8	<12.8	<12.8	<12.8
Herschel/SPIRE 250 μm	[mJy]	(17.9 ± 5.0)[♯]	(18.5 ± 5.0)[♯]	<14.4	(21.1 ± 5.0)[♯]	<14.4
Herschel/SPIRE 350 μm	[mJy]	(19.9 ± 5.7)[♯]	(21.4 ± 5.7)[♯]	<16.5	(19.3 ± 5.7)[♯]	<16.5
Herschel/SPIRE 500 μm	[mJy]	(15.3 ± 6.3)[♯]	(15.3 ± 6.3)[♯]	<18.3	(13.0 ± 6.3)[♯]	<18.3
JVLA 6 GHz	[μJy]	12.0 ± 2.9	<2.16	10.9 ± 2.8	23.0 ± 2.5	<2.16
VLA 1.4 GHz	[μJy]	<24	<24	<24	50.9 ± 7.45	<24

*Inequality signs represent the 3σ limits of photometry. We did not use Subaru data in SXDF-ALMA3 because of the contamination from a nearby source.

[†]The sky positions of our ALMA sources adopted from K. Kohno et al. (in preparation).

[‡]The 1.1 mm observed peak flux densities (primary beam collected) presented in K. Kohno et al. (in preparation).

[§]The 1.1 mm observed spatially integrated flux densities (primary beam collected) presented in K. Kohno et al. (in preparation).

[‖]The sky positions of $F160W$ counterparts derived from $F160W$-selected catalog (Galametz et al. 2013).

[♯]SPIRE photometry using the HIPE task `sourceExtractorSussextractor` at the ALMA position. The errors were estimated by adding the 1σ confusion errors and instrumental errors in the quadrature.

map was processed with the CLEAN algorithm (Högbom 1974) using natural weighting.

The resulting image had a 1σ sensitivity of 0.048–0.061 mJy beam^{-1}, and the typical noise level was 0.055 mJy beam^{-1} (Hatsukade et al. 2016; K. Kohno et al. in preparation). From the ALMA map, we extracted five significant sources with a signal-to-noise ratio of $S/N > 5$ (hereafter SXDF-ALMA1, 2, 3, 4, and 5; see table 1, and also Kohno et al. 2016).[2] Two of the five sources (SXDF-ALMA1 and 2) were detected as a single bright SMG ($S_{1.1mm} = 3.5^{+0.6}_{-0.5}$ mJy) with the Astronomical Thermal

Emission Camera (AzTEC: Wilson et al. 2008)/Atacama Submillimeter Telescope Experiment (ASTE: Ezawa et al. 2004) 1.1 mm survey in SXDF (S. Ikarashi et al. in preparation).

2.2 Optical-to-near-infrared images

In order to characterize the stellar properties of the ALMA sources, we used archival optical-to-near-infrared images collected by ground-based and space-borne facilities such as Subaru, the Very Large Telescope (VLT), the Hubble Space Telescope (HST), and the Spitzer Space Telescope (Spitzer). We describe the details of the optical/near-infrared data below.

[2] Hatsukade et al. (2016) report on an additional source with $S/N = 5$, which is detected as SXDF-ALMA6 with $S/N = 4.7$ in Kohno et al. (2016). We do not discuss this source in a multiwavelength context here, because it has no counterpart in multiwavelength images.

2.2.1 Ground-based telescopes

Optical ground-based imaging observations of the UDS field were made with Subaru/Suprime-Cam (Miyazaki et al. 2002) using five wideband filters ($BVR_\mathrm{C}i'z'$) as part of Subaru/XMM-Newton Deep Survey (Furusawa et al. 2008). These data reached 3σ limiting magnitudes of $B = 28.4$, $V = 27.8$, $R_\mathrm{C} = 27.7$, $i' = 27.7$, and $z' = 26.6$ with a $1''$ radius aperture (Furusawa et al. 2008).

The CANDELS UDS field was also observed as part of the HAWK-I UDS and GOODS-S survey (HUGS; VLT large program ID: 186.A-0898, Fontana et al. 2014) with two near-infrared broadband filters (Y and K_s). The data reached 5σ limiting magnitudes of $Y = 27.05$ and $K_\mathrm{s} = 26.16$ with $0''.42$ and $0''.36$ radius apertures (Galametz et al. 2013).

2.2.2 HST

The HST data were taken with the Advanced Camera for Surveys (ACS: Ford et al. 1998)/*F606W* and ACS/*F814W* together with the Wide Field Camera 3 (WFC3: Kimble et al. 2008)/*F125W* and WFC3/*F160W*. The final UDS HST images are publicly available via the STScI archive.[3] These images reached 5σ limiting magnitudes of ACS/*F606W* = 26.74, ACS/*F814W* = 26.67, WFC3/*F125W* = 26.80, and WFC3/*F160W* = 26.91 with a $0''.7$ radius aperture, respectively (Koekemoer et al. 2011).

2.2.3 Spitzer/IRAC

We use Spitzer/InfraRed Array Camera (IRAC: Fazio et al. 2004) data. Channel 1 ($3.6\,\mu$m) and Channel 2 ($4.5\,\mu$m) data were from the Spitzer Extended Deep Survey (SEDS; PI: G. Fazio; Ashby et al. 2013), and Channel 3 ($5.6\,\mu$m) and Channel 4 ($8.0\,\mu$m) data were from the Spitzer UKIDSS Ultra Deep Survey (SpUDS; PI: J. Dunlop; Caputi et al. 2011). These images at 3.6, 4.5, 5.8, and $8.0\,\mu$m reached 5σ limiting magnitudes of 24.72, 24.61, 22.30, and 22.26 with $1''.9$, $1''.9$, $2''.08$, and $2''.20$ radius apertures, respectively (Galametz et al. 2013).

2.3 Mid-infrared-to-radio images

Here, we summarize mid-infrared to radio images, which we retrieved from public archives.

2.3.1 Spitzer/MIPS

We also used the Multiband Imaging Photometer for the Spitzer (MIPS: Rieke et al. 2004) $24\,\mu$m image from SpUDS. The final Spitzer/MIPS image is publicly available via the NASA/IPAC Infrared Science Archive.[4] The image reached

a 3σ limiting magnitude of 19.9 (details of our photometry are explained in subsection 3.2).

2.3.2 Herschel/PACS and SPIRE

The far-infrared to submillimeter Herschel images were taken with the Photodetector Array Camera and Spectrometer (PACS) at 100 and $160\,\mu$m (Poglitsch et al. 2010) and with the Spectral and Photometric Imaging Receiver (SPIRE) at 250, 350, and $500\,\mu$m (Griffin et al. 2010) as part of the Herschel Multi-tiered Extragalactic Survey (HerMES;[5] see Oliver et al. 2012, for details). These images were retrieved from the Herschel Science Archive. The 5σ instrument sensitivities at 100, 160, 250, 350, and $500\,\mu$m (ignoring confusion noise) was 6.8, 12.9, 11.2, 9.3, and 13.4 mJy, respectively (Oliver et al. 2012). Note that Herschel/SPIRE on sky images is dominated by confusion noise because of the large beam size ($18''.1$, $25''.2$, and $36''.6$ for 250, 350, and $500\,\mu$m; Griffin et al. 2010). In HerMES, the confusion noise of Herschel/SPIRE is calculated from images of the GOODS-N, Lockman-North, and Lockman-SWIRE fields (Nguyen et al. 2010). Here, we adopted their confusion noises of $5\sigma = 24.0$, 27.5, and 30.5 mJy at 250, 350, and $500\,\mu$m, respectively.

2.3.3 Radio images

Radio images at 1.4 GHz and 6 GHz were obtained by using the Very Large Array (VLA) and the Karl G. Jansky Very Large Array (JVLA), respectively.

The details of the VLA 1.4 GHz observations are given by V. Arumugam et al. (in preparation). The synthesized beam size for this 1.4 GHz image was $1''.8 \times 1''.6$ with the position angle of $-3°$. The 1.4 GHz image reached a 1σ uncertainty of $8\,\mu$Jy. On the other hand, the JVLA 6 GHz observations are presented by K. Tadaki et al. (in preparation). The synthesized beam size was $0''.5 \times 0''.4$ with the position angle of $-3°$. The 6 GHz image reached a 1σ uncertainty of $0.72\,\mu$Jy.

2.4 X-ray images

Ueda et al. (2008) presented an X-ray source catalog for the SXDF-UDS-CANDELS field using the XMM-Newton satellite. The sensitivity limits of the catalog in the 0.5–2, 0.5–4.5, 2–10, and 4.5–10 keV bands reached 6×10^{-16}, 8×10^{-16}, 3×10^{-15}, and 5×10^{-15} erg cm^{-2} s^{-1}, respectively. The five ALMA sources are not listed in the catalog.

---

[3] ⟨https://archive.stsci.edu/prepds/candels/⟩.

[4] ⟨http://irsa.ipac.caltech.edu/data/SPITZER/SpUDS/⟩.
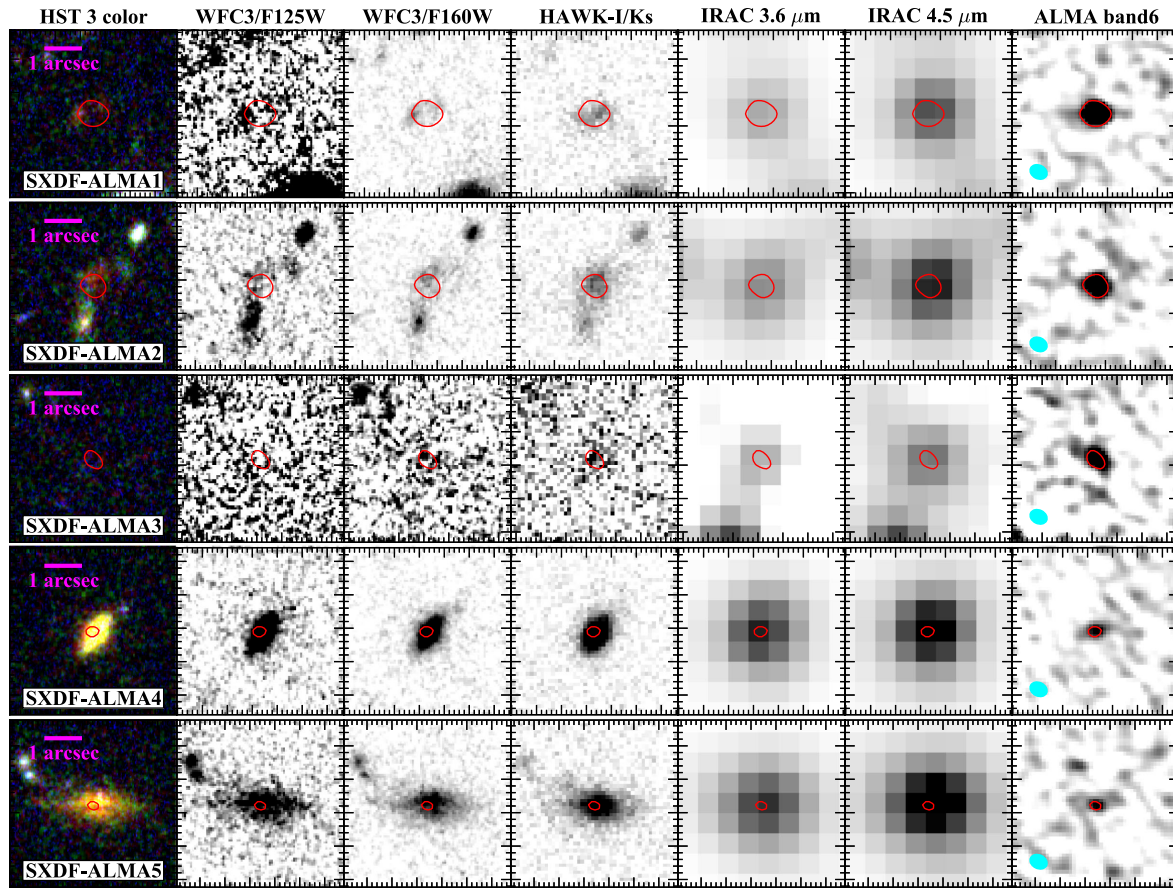
[5] ⟨http://hermes.sussex.ac.uk/⟩.

Fig. 1. Optical-to-near-infrared images of our ALMA sources. From left to right: HST three-color (R: WFC3/*F160W*, G: WFC3/*F125W*, B: ACS/*F814W*), HST WFC3/*F125W*, HST WFC3/*F160W*, VLT HAWK-I/K_s, Spitzer IRAC/3.6 μm, Spitzer IRAC/4.5 μm, and ALMA 1.1 mm images ($5'' \times 5''$). The solid red contours indicate the ALMA 1.1 mm detection at the 5σ level. The synthesized beams are presented in the bottom left of the ALMA images (cyan).

3 Counterpart identification and photometry

3.1 Optical-to-near-infrared counterparts and photometry

Figure 1 shows the HST three-color image (for red, WFC3/*F160W*; for green, WFC3/*F125W*; for blue, ACS/*F814W*), WFC3/*F125W*, WFC3/*F160W*, HAWK-I/K_s, Spitzer/IRAC 3.6 μm, 4.5 μm, and ALMA Band 6 images overlaid with the ALMA contours. All of five ALMA sources had counterparts in at least four independent bands. The WFC3/*F160W* counterparts to four of the five ALMA sources (SXDF-ALMA1, 2, 4, and 5) were already identified in the catalog presented by Galametz et al. (2013) ($H \simeq 22.4$–24.5). Although SXDF-ALMA3 is not cataloged in Galametz et al. (2013), it was marginally detected (4.2σ, $H = 25.30 \pm 0.25$) with WFC3/*F160W* (details of our photometry are explained later in this section). We found that SXDF-ALMA1 and SXDF-ALMA2 coincide with the cataloged Hα emitters (HAEs) having narrowband redshifts of $z = 2.53 \pm 0.02$ (Tadaki et al. 2013).

We used the Image Reduction and Analysis Facility (IRAF: Tody 1993) to measure the flux densities of the

counterparts in the optical-to-near-infrared images. First, to account for the point spread function (PSF) difference between images, images were PSF-matched using the IRAF task GAUSS. Except for the Spitzer/IRAC images, we adopted the Gaussian PSF with a full width at half maximum of $1''$. Spitzer/IRAC images were PSF-matched to the 8.0 μm band image, which had the poorest angular resolution among the IRAC bands at $2''.2$.

Next, we performed optical-to-near-infrared photometry with a $2''$ diameter aperture at the position of the ALMA sources using the IRAF task APPHOT. We made the aperture correction using the same procedure described by Ono et al. (2010). We measured fluxes for 20 bright point sources in a series of diameter apertures from $2''$ up to $6''$ with an interval of $0''.1$. Since we found that the fluxes level off for $>5''$ diameter apertures, we defined $5''$ diameter aperture magnitudes as total magnitudes. Then, we selected 100 point sources, measured fluxes over $2''$ and $5''$ diameter apertures, and calculated an accurate offset between these two aperture magnitudes as the aperture correction term. We estimated the flux uncertainties by using the SDFRED (Yagi et al. 2002;
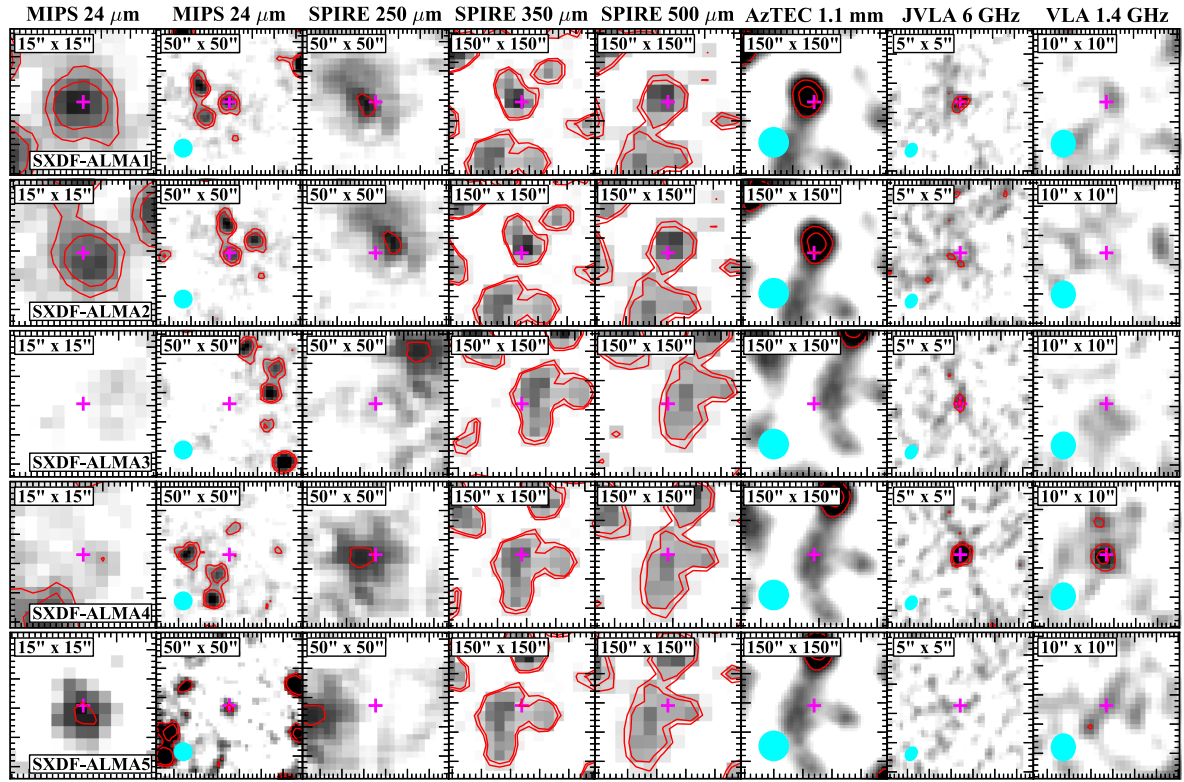
Fig. 2. Mid-infrared-to-radio images of SXDF-ALMA1, 2, 3, 4, and 5 (from top to bottom). From left to right: $15'' \times 15''$ image of Spitzer/MIPS 24 μm; $50'' \times 50''$ images of Spitzer/MIPS 24 μm and Herschel/SPIRE 250 μm, $150'' \times 150''$ images of Herschel/SPIRE 350, 500 μm, and AzTEC/ASTE 1.1 mm; $5'' \times 5''$ image of JVLA 6 GHz; $10'' \times 10''$ image of VLA 1.4 GHz. The magenta crosses mark the ALMA positions. The beam sizes of MIPS 24 μm, AzTEC/ASTE, JVLA, and VLA are shown by cyan symbols. Red solid lines indicate the contours (3σ and 5σ) of the images.

Ouchi et al. 2004) task `LIMITMAG`. Table 1 lists the photometry results.

Note that Tadaki et al. (2015) used the optical-to-near-infrared photometry of SXDF-ALMA1 and 2 from the photometry catalog presented by Skelton et al. (2014), which follows a different photometric procedure from ours. We did not use their photometry because we preferred comparing all of the ALMA sources in the same manner.

3.2 Mid-infrared-to-radio counterparts and photometry

Figure 2 shows Spitzer/MIPS 24 μm, Herschel/SPIRE 250, 350, 500 μm, AzTEC/ASTE 1.1 mm, JVLA 6 GHz, and VLA 1.4 GHz images of the ALMA sources. For the MIPS 24 μm image, we performed aperture photometry with a $3''$ aperture radius. The MIPS instrument handbook[6] was used to calculate the aperture correction for the missing flux outside the aperture. For the Herschel/SPIRE bands, we used the Herschel Interactive Processing Environment (HIPE: Ott 2010) to perform the `sourceExtractorSussextractor` task at the ALMA source positions. Note that, because

---

[6] ⟨http://irsa.ipac.caltech.edu/data/SPITZER/docs/mips/mipsinstrumenthandbook/⟩.

the SPIRE photometry listed in table 1 is highly likely to be affected by blending with nearby infrared sources, the nominal values should be considered as upper limits. In the VLA 1.4 GHz and JVLA 6 GHz images we measured the flux densities with two-dimensional Gaussian fitting by using the Astronomical Image Processing System (`AIPS`; van Moorsel et al. 1996) to perform the `JMFIT` task. For non-detection, we set a 3σ upper limit. Table 1 summarizes the results. We present the mid-infrared-to-radio properties of individual ALMA sources below.

- SXDF-ALMA1 and 2: SXDF-ALMA1 and 2 are close to each other and the separation is $\sim 10''$, which may cause significant blending with each other in the mid-infrared-to-far-infrared bands. They both were detected at 24 μm (18.66 ± 0.12 mag and 18.82 ± 0.13 mag, respectively). In the SPIRE images, it is likely that SXDF-ALMA1, 2, and a nearby MIPS source are blended, which resulted in a single cataloged SPIRE source of J021740.9−051309 (Oliver et al. 2012). Therefore, we simply placed 5σ upper limits on the SPIRE photometry at the positions of SXDF-ALMA1 and 2. The sum of the 1.1 mm flux density of the two sources ($S_{1.1mm} = 3.4 \pm 0.2$ mJy) showed good agreement with the flux density of the blended AzTEC/ASTE

Table 2. Results of the multiwavelength analysis.

		SXDF-ALMA1	SXDF-ALMA2	SXDF-ALMA3	SXDF-ALMA4	SXDF-ALMA5
z_{photo}[*]	(EAZY)	$2.27^{+0.94}_{-0.87}$	$2.54^{+0.23}_{-0.51}$	$2.4^{+2.5}_{-2.0}$	$1.33^{+0.10}_{-0.16}$	$1.52^{+0.13}_{-0.18}$
z_{photo}[†]	(HYPERZ)	$2.94^{+0.45}_{-0.32}$	$2.06^{+0.21}_{-0.08}$	$3.1^{+3.9}_{-1.8}$	$1.39^{+0.02}_{-0.02}$	$1.63^{+0.03}_{-0.02}$
z_{NB}[‡]		2.53 ± 0.02	2.53 ± 0.02	—	—	—
M_*[§]	$[\times 10^{10}\, M_\odot]$	$9.5^{+2.8}_{-7.3}$	$9.3^{+1.1}_{-6.7}$	—	$3.5^{+1.6}_{-0.9}$	$4.1^{+3.2}_{-2.2}$
A_V[§]	[mag]	$2.6^{+1.9}_{-1.5}$	$1.6^{+0.1}_{-0.8}$	—	$1.9^{+0.6}_{-1.0}$	$2.3^{+0.7}_{-1.5}$
L_{IR}[‖]	$[\times 10^{12}\, L_\odot]$	2^{+2}_{-1}	$1^{+1}_{-0.8}$	$1^{+1}_{-0.7}$	$0.3^{+0.2}_{-0.2}$	$0.5^{+0.5}_{-0.4}$
SFR_{UV}[♯]	$[M_\odot\, yr^{-1}]$	<2	6 ± 2	—	0.6 ± 0.2	1 ± 0.4
SFR_{IR}[**]	$[M_\odot\, yr^{-1}]$	200^{+200}_{-100}	100^{+100}_{-80}	100^{+100}_{-70}	30^{+20}_{-20}	50^{+50}_{-40}
$SFR_{UV + IR}$[††]	$[M_\odot\, yr^{-1}]$	200^{+200}_{-100}	100^{+100}_{-80}	—	30^{+20}_{-20}	50^{+50}_{-40}
$sSFR$[‡‡]	$[Gyr^{-1}]$	2^{+2}_{-2}	1^{+1}_{-1}	—	$0.8^{+0.6}_{-0.6}$	1^{+2}_{-1}

[*]Photometric redshifts with 99% confidence intervals calculated by using EAZY with flux- and redshift-based priors.

[†]Photometric redshifts with 99% confidence intervals calculated by using HYPERZ.

[‡]Narrowband redshifts derived from Hα observations (Tadaki et al. 2013).

[§]Stellar masses and visual extinction estimated from the SED fitting code FAST with 99% confidence intervals.

[‖]Infrared luminosities based on the mid-infrared-to-far-infrared SED templates by Dale and Helou (2002). See the Appendix for details.

[♯]SFRs obtained from their infrared luminosities.

[**]SFRs obtained from their infrared luminosities.

[††]$SFR_{UV} + SFR_{IR}$.

[‡‡]sSFRs obtained from their $SFR_{UV + IR}$ and stellar masses.

source ($S_{1.1mm} = 3.5^{+0.6}_{-0.5}$ mJy; S. Ikarashi et al. in preparation). SXDF-ALMA1 was detected at 6 GHz ($S_{6GHz} = 12.0 \pm 2.9$ μJy), but SXDF-ALMA2 had no counterpart in the radio images.

- SXDF-ALMA3: SXDF-ALMA3 was only detected at 6 GHz ($S_{6GHz} = 10.0 \pm 2.8$ μJy). The interpretation is given in the following sections.

- SXDF-ALMA4: This object was detected not at 24 μm but at 6 GHz and 1.4 GHz with 23.0 ± 2.5 μJy and 50.09 ± 7.45 μJy, respectively. In the SPIRE bands, this source was heavily blended with a nearby 24 μm source (with a separation of $\sim 8''$), and the blended source was identified as J021742.5−051406 (Oliver et al. 2012).

- SXDF-ALMA5: SXDF-ALMA5 was detected in the MIPS 24 μm band (19.53 ± 0.26 mag), although it was not detected in the Herschel or radio images.

4 Multiwavelength SED

4.1 SED fitting at optical-to-near-infrared wavelengths

4.1.1 Photometric redshift calculation

We estimated the photometric redshifts of the ALMA sources. To derive the photometric redshifts and check their reliability, we used two different SED fitting codes: HYPERZ (Bolzonella et al. 2000) and EAZY (Brammer et al. 2008). They both compute the χ^2 statistic for a set of SED models to the observed photometry, but EAZY includes the optional flux- and redshift-based priors (for details, see Brammer

et al. 2008). Confidence intervals were obtained by integrating the posterior redshift probability distributions (for details, see Brammer et al. 2008). The following parameters were considered for SED fitting. The redshift range was set to $z = 0$–7. Extinction was considered with the range of $A_V = 0$–5 mag in increments of 0.5 mag, and we adopted the Calzetti extinction law (Calzetti et al. 2000). For HYPERZ, we utilized the SED templates of Bruzual and Charlot (1993) for elliptical, Sb, burst, constant, and star formation (Im). For EAZY, SED templates of Bruzual and Charlot (2003, hereafter BC03) were used. In the case of nondetection, we adopted the nominal photometric value with 1σ uncertainty during the SED fitting.

Table 2 summarizes the derived photometric redshifts. Figure 3 shows the best-fitting SEDs of the ALMA sources. Throughout this paper, we use the 99% confidence intervals to represent the uncertainty of the photometric redshift estimates, as done in previous works (e.g., Wardlow et al. 2011; Simpson et al. 2014). The photometric redshifts estimated by HYPERZ and EAZY agreed within the errors, and no systematic offsets between the two were found. Note that the photometric redshift errors derived by HYPERZ tend to be underestimated because the χ^2 distribution is not a realistic description of the true photometric redshift error distribution (Oyaizu et al. 2008). Therefore, we discuss the results from EAZY in the following sections.

Consequently, we obtained the photometric redshifts of SXDF-ALMA1, 2, 4, and 5 ($z_{photo} = 2.27^{+0.94}_{-0.87}$, $2.54^{+0.23}_{-0.51}$, $1.33^{+0.10}_{-0.16}$, and $1.52^{+0.13}_{-0.18}$, respectively), while that of SXDF-ALMA3 was poorly constrained ($z_{photo} = 2.4^{+2.5}_{-2.0}$) because
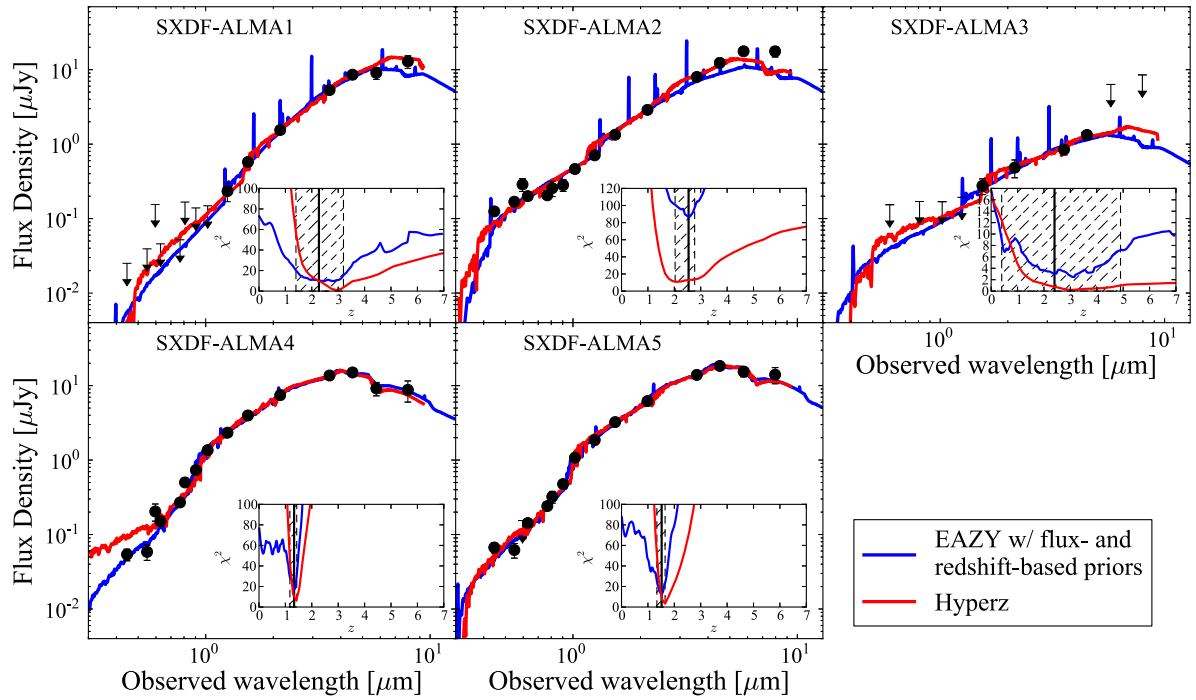
Fig. 3. Photometry and best-fitting SEDs for SXDF-ALMA1, 2, 3, 4, and 5. The dots with error bars are photometric data points, whereas the arrows indicate 3σ upper limits. The blue and red lines indicate the results calculated with EAZY and HYPERZ, respectively. The inset panel in each plot shows the χ^2 distribution as a function of the redshift and indicates the best-fitting photometric redshift as estimated by EAZY with a black solid line. The hatched region shows the 99% confidence interval estimated with EAZY.

of the limited number of detections lacking significant break features. The photometric redshifts of SXDF-ALMA1 and 2 were consistent with their narrowband Hα redshifts ($z_{NB} = 2.53 \pm 0.02$; see table 2) for the EAZY solutions.

4.1.2 Estimation of stellar masses

We estimated the stellar masses of SXDF-ALMA1, 2, 4, and 5, for which reliable SED fits were obtained. The SED fitting at optical-to-near-infrared wavelengths was done by using the FAST code (Kriek et al. 2009), which is compatible with EAZY, to derive the stellar masses. In the SED fitting, the templates were taken from the population synthesis model of BC03 with a solar metallicity in accordance with previous research on faint SMGs (e.g., Tadaki et al. 2015). Here, we assumed the Chabrier initial mass function (IMF: Chabrier 2003), the Calzetti extinction law, and exponentially declining star formation histories. Following the recipe presented by Wuyts et al. (2011), we used the e-folding timescale of SFRs $\tau \geq 300$ Myr for fitting. This is because Wuyts et al. (2011) suggested that setting $\tau \geq 300$ Myr yields the most reasonable SED fits for star-forming galaxies. For SXDF-ALMA1 and 2, we fixed the redshifts to the narrowband redshifts, while we used the photometric redshifts estimated by EAZY for SXDF-ALMA4

and 5. Table 2 summarizes the results from the SED fitting using FAST.

To constrain the stellar mass of SXDF-ALMA3, we derived it by using a mass-to-light ratio obtained in the rest-frame H-band, as done in previous works (e.g., Hainline et al. 2011; Wardlow et al. 2011; Simpson et al. 2014). There are several benefits of using a rest-frame H-band magnitude. The cooler low-mass stars that dominate the stellar mass of a galaxy emit most of their light at red optical and near-infrared wavelengths. In addition, the rest-frame H-band is less sensitive to dust extinction than rest-frame optical bands and is less affected by thermally pulsating asymptotic giant branch stars than the rest-frame K-band according to Hainline et al. (2011), who utilized BC03 SED templates with Chabrier IMF and obtained $M_*/L_H = 0.17$ and $0.13\ M_\odot\ L_\odot^{-1}$ for constant and single-burst star formation histories, respectively (L_H is the rest-frame H-band luminosity without extinction correction). Here, we adopted the average value $M_*/L_H = 0.15\ M_\odot\ L_\odot^{-1}$ of these two extreme cases. If we assumed that SXDF-ALMA3 lies at $z = 2$, 3, or 4 and used L_H obtained from the rest-frame H-band magnitudes in table 2, the stellar mass was estimated to be $\sim 5 \times 10^9$, $< 2 \times 10^{10}$, or $< 6 \times 10^{10}\ M_\odot$ (the inequality sign represents the 3σ upper limit). Despite the redshift uncertainty, the constraints favored a lower stellar mass for SXDF-ALMA3 than that for the other ALMA
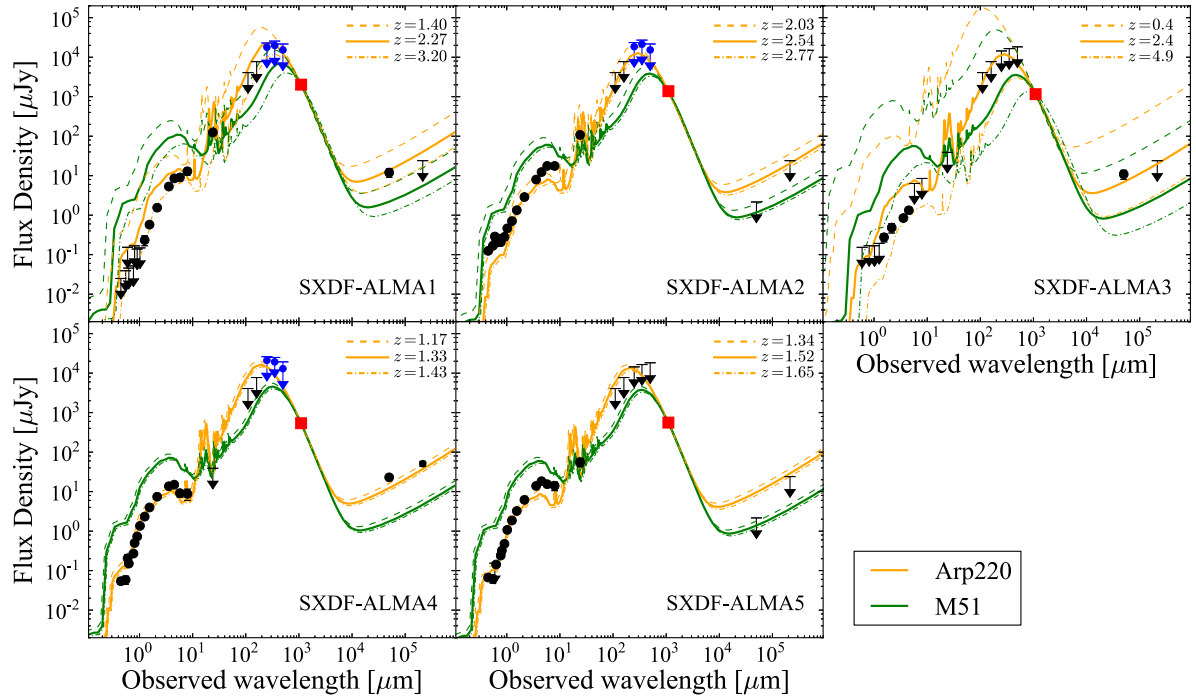
Fig. 4. Optical-to-radio SED of SXDF-ALMA1, 2, 3, 4, and 5. The red squares show 1.1 mm flux densities. The black dots indicate photometric data points at the optical-to-radio wavelengths. The black arrows represent 3σ upper limits. When SPIRE photometry suffered from heavy contamination of nearby sources (SXDF-ALMA1, 2, and 4), we plotted nominal values of SPIRE photometry as upper limits (see subsection 3.2). For comparison, we plotted SED templates of Arp 220 and M 51 (Silva et al. 1998). The SED templates were scaled to the flux densities at 1.1 mm. The redshifts were fixed to the best-fitting values estimated by EAZY (solid lines) and the lower and upper limits of the 99% confidence intervals.

sources. This can be one of the reasons why it is faint at optical-to-near-infrared wavelengths.

4.2 Estimation of SFRs

We computed their SFRs by summing the ultraviolet SFRs (SFR_{UV}) and infrared SFRs (SFR_{IR}) based on the work of Kennicutt (1998):

$$SFR_{UV+IR}(M_\odot\,yr^{-1}) = (3.3L_{2800} + L_{IR})/L_\odot \times 10^{-10}, \quad (1)$$

where L_{2800} is the rest-frame 2800 Å luminosity. To derive their total infrared luminosities, we used the mid-infrared-to-far-infrared SED templates from Dale and Helou (2002), which are often applied to dusty star-forming galaxies observed by Herschel (e.g., Chapman et al. 2010; Magnelli et al. 2014; Ilbert et al. 2015), scaled to the observed flux densities at 1.1 mm ($S_{1.1mm;total}$). We assumed dust temperatures of $T_{dust} = 20$–$35\,K$ (for SXDF-ALMA4, $T_{dust} = 20$–$30\,K$; see the Appendix for details) and an emissivity index $\beta = 1.5$, which is a typical value for $z \sim 1$–2 star-forming galaxies (e.g., Elbaz et al. 2011; Symeonidis et al. 2013).

To consider a variety of SEDs, we also estimated L_{IR} by assuming the template SED of the well-studied starburst galaxy Arp 220 (Silva et al. 1998) and a typical

SED of SMGs from Pope et al. (2008). We found that the values obtained were within the uncertainties presented in table 2. Note that we only used the observed flux densities at 1.1 mm. Therefore, the derived values should have large systematic uncertainties. We also obtained sSFR by using their ultraviolet + infrared SFRs and stellar masses. Table 2 summarizes the derived values.

4.3 Optical-to-radio SED

Figure 4 plots the optical-to-radio SEDs of the ALMA sources. Because SXDF-ALMA1, 2, and 4 suffered from heavy contamination in the Herschel SPIRE photometry (see subsection 3.2 and figure 2), we plotted nominal values of SPIRE photometry with the blue dots with arrows, which should be regarded as upper limits. For comparison, we also plotted two different template SEDs modeled by Silva et al. (1998): a dusty starburst galaxy (Arp 220) and spiral galaxy (M 51). They also differ in dust temperature: $T_{dust} = 47\,K$ for Arp 220 (Klaas et al. 1997) and $T_{dust} = 24.9\,K$ for M 51 (Mentuch Cooper et al. 2012). For the solid lines, the redshifts were fixed to the best-fitting photometric redshifts estimated by EAZY. To account for the redshift uncertainties, we also plotted the template SEDs for which the redshift was fixed to the lower and upper boundaries of the

99% confidence intervals. These SEDs were scaled to the flux densities at 1.1 mm.

As shown in figure 4, the photometric redshifts from optical-to-near-infrared photometry and resulting SEDs extended to far-infrared produced a reasonable model for the dust emission. The optical-to-radio SEDs of the ALMA sources seem to match Arp 220 better than M 51. In particular, the rest-frame ultraviolet+optical SEDs show evidence for more obscured young stellar population than the local disk galaxies like M 51, as expected. Previously, da Cunha et al. (2015) have suggested that the average SED of SMGs identified in the ALMA follow-up observation of the LABOCA Extended Chandra Deep Field South surveys (ALESS: Hodge et al. 2013) is inconsistent with Arp 220, especially in the optical to near-infrared wavelengths. The SEDs of these ALMA sources are more like those of the local ultra-luminous infrared galaxies than ALESS SMGs.

As shown in figure 2, SXDF-ALMA1, 2, and 4 were heavily blended with nearby MIPS sources in the Herschel/SPIRE bands, which suggests that their flux densities were overestimated. At $z \sim 1.3$, a silicate absorption feature at rest-frame 9.7 μm shifted into the MIPS 24 μm band. This may be why SXDF-ALMA4 was not detected at MIPS 24 μm. The local (ultra-)luminous infrared galaxies exhibited a broad silicate absorption feature at rest frame 9.7 μm (e.g., Armus et al. 2007; Pereira-Santaella et al. 2010). The silicate absorption feature is known to merely require a mass of warm dust obscured by a significant column of cooler dust (e.g., Magdis et al. 2011). SXDF-ALMA4 was detected at 1.4 GHz, and the photometry is consistent with the SED template of Arp 220. This suggests that the dust temperature is higher than the assumed $T_{\rm dust} = 20$–30 K (see the Appendix for details).

The far-infrared-to-radio SED of SXDF-ALMA3 may place a more stringent constraint on the redshift than the optical/near-infrared photometric one. As shown in figure 4, the upper limits and 6 GHz photometry suggest that this object is located at $z \simeq 2$–3 if the SED is similar to M 51 and Arp 220.

5 Discussion

5.1 Contribution to the infrared extragalactic background light

Owing to the high sensitivity and high angular resolution observations with ALMA, 50%–100% of the infrared extragalactic background light has been claimed to be resolved if we go down to $\sim$0.1–0.02 mJy (e.g., Hatsukade et al. 2013; Ono et al. 2014; Carniani et al. 2015; Fujimoto et al. 2016). From the summation of the 1.1 mm flux densities of all of our ALMA sources and

the survey area (2 arcmin^2), the contribution of the ALMA sources to the infrared extragalactic background light was estimated to be $\sim 10^{+6}_{-4}$ Jy deg^{-2}, which corresponds to $\sim 40^{+24}_{-16}$% of the infrared extragalactic background light obtained by Fixsen et al. (1998) using the COsmic Background Explore (COBE) satellite (25^{+22}_{-13} Jy deg^{-2}; Carniani et al. 2015) or $\sim 54^{+32}_{-22}$% if we adopt the COBE measurement made by Puget et al. (1996, 18.5 Jy deg^{-2}). In the subsequent discussion, we adopt the Fixsen et al. (1998)'s value for the infrared extragalactic background light, but we caution that there exist uncertainties (likely systematic) in the COBE measurements. Because of the numbers of our sources, we used the Poisson uncertainty values presented by Gehrels (1986). The completeness in the flux range of ALMA sources was $\sim$100% (Hatsukade et al. 2016).

Note that this value can be overestimated because our observation field was selected to include a single bright SMG (S. Ikarashi et al. in preparation) and a chain of HAEs at $z = 2.5$ (Tadaki et al. 2013, 2015). Given that SXDF-ALMA1 and 2 were identified as an AzTEC/ASTE source (S. Ikarashi et al. in preparation) and HAEs (Tadaki et al. 2013), it is better to exclude SXDF-ALMA1 and 2 when discussing the real contribution of the ALMA sources to the infrared extragalactic background light. The contributions of SXDF-ALMA3, 4, and 5 to the infrared extragalactic background light were estimated to be $\sim 4.1^{+5.4}_{-3.0}$ Jy deg^{-2}, which corresponds to $\sim 16^{+22}_{-12}$% of the infrared extragalactic background light obtained by the COBE satellite. This suggests that their contribution to the infrared extragalactic background light is as large as that of bright SMGs ($S_{1.1\rm mm} \geq 1.0$ mJy, $\sim$2.9 Jy deg^{-2}; Hatsukade et al. 2011). Although our survey area is small and may have been affected by cosmic variance, these results suggest that bright ($S_{1.1\rm mm} \geq 1$ mJy) sources and faint SMGs with 0.5 mJy $< S_{1.1\rm mm} \lesssim 1.0$ mJy, which is the flux range of the ALMA source, seem to contribute $\sim 28^{+22}_{-12}$% to the infrared extragalactic background light. These results suggest that faint SMGs with $S_{1.1\rm mm} \lesssim 0.5$ mJy are major contributors to the infrared extragalactic background light. The results of stacking analysis of near-infrared selected galaxies with $S_{1.1\rm mm} \lesssim 0.5$ mJy will be discussed in our upcoming paper (W. Wang et al. in preparation).

5.2 Contribution to the cosmic SFRD

Substantial attempts have been made with Herschel to resolve the redshift evolution of the contribution of infrared selected galaxies up to $z = 3$ (Burgarella et al. 2013). Burgarella et al. (2013) estimated the cosmic infrared SFRD from the infrared luminosity functions inferred from Herschel observations and found that the contribution peaks

at $z = 1.35$, which accounts for 89% of the total cosmic SFRD of $1.1 \times 10^{-1}\,M_\odot\,\mathrm{yr}^{-1}\,\mathrm{Mpc}^{-3}$ (using Chabrier IMF). However, they used the extrapolate infrared luminosity functions below the confusion limit of Herschel (e.g., $L_{\mathrm{IR}} \lesssim 10^{12}\,L_\odot$ at $z \simeq 2$) to estimate the cosmic infrared SFRD. Wardlow et al. (2011) derived infrared luminosity functions of SMGs detected by the LABOCA Extended Chandra Deep Field South surveys (LESS: Weiß et al. 2009). However, they did not also investigate the luminosity range of $L_{\mathrm{IR}} \lesssim 10^{12}\,L_\odot$.

ALMA sources with (photometric) redshifts allow the constraint on the contribution from a faint ($L_{\mathrm{IR}} \lesssim 10^{12}\,L_\odot$) population of star-forming galaxies. In addition, the contribution from galaxies undetected by Herschel can be estimated. We simply assume that the ALMA sources lie in the redshift interval of $1 < z < 4$ (co-moving volume: $V_{\mathrm{com}} \sim 1.9 \times 10^4\,\mathrm{Mpc}^3$) to cover the redshift uncertainties of the ALMA sources. Then, we estimate the contribution from all of the ALMA sources, including SXDF-ALMA1 and 2, on the basis of SFRs simply derived from the 1.1 mm flux densities (subsection 4.2). Considering the uncertainty in T_{dust} (see subsection 4.2 and the Appendix), the inferred infrared SFRD for $1 < z < 4$ is $\sim (0.9–5) \times 10^{-2}\,M_\odot\,\mathrm{yr}^{-1}\,\mathrm{Mpc}^{-3}$, which accounts for $\sim 10\%$–70% of the average infrared SFRD at $0.9 < z < 3.6$ as estimated by Herschel (using Chabrier IMF, $\sim 7 \times 10^{-2}\,M_\odot\,\mathrm{yr}^{-1}\,\mathrm{Mpc}^{-3}$; Burgarella et al. 2013). If we exclude SXDF-ALMA1 and 2 to avoid the contribution of the known AzTEC source, then the infrared SFRD for $1 < z < 4$ is estimated to be $\sim (0.3–2) \times 10^{-2}\,M_\odot\,\mathrm{yr}^{-1}\,\mathrm{Mpc}^{-3}$. The inferred cosmic infrared SFRD is similar to that of bright SMGs ($S_{870\mu m} > 4\,\mathrm{mJy}$) at $z \simeq 2$–3 [$\sim (1–2) \times 10^{-2}\,M_\odot\,\mathrm{yr}^{-1}\,\mathrm{Mpc}^{-3}$ using Chabrier IMF; Wardlow et al. 2011]. These results imply that the ALMA sources play an important role in the cosmic SFRD, even if we exclude the contribution of the known AzTEC source at $1 < z < 4$. Note that our results can be affected by the cosmic variance and clustering because of our small survey area. Therefore, future ALMA large surveys will provide a stronger constraint on the role of faint SMGs in the cosmic SFRD.

Chen et al. (2014) inferred that there are many submillimeter sources that are sources difficult to detect in deep optical/near-infrared surveys like SXDF-ALMA3. Indeed, submillimeter sources which have no counterparts at optical/near-infrared wavelengths have been reported (e.g., Wang et al. 2007; Smolčić et al. 2012; Simpson et al. 2014; Dunlop et al. 2016). However, their real contributions to the cosmic infrared SFRD are uncertain. The contribution of SXDF-ALMA3 to the cosmic infrared SFRD may be $\sim (0.1–1) \times 10^{-2}\,M_\odot\,\mathrm{yr}^{-1}\,\mathrm{Mpc}^{-3}$ or $\sim 1\%$–10% of the average infrared SFRD at $0.9 < z < 3.6$ as estimated

by Herschel ($\sim 7 \times 10^{-2}\,M_\odot\,\mathrm{yr}^{-1}\,\mathrm{Mpc}^{-3}$) if this object lies somewhere in the redshift interval of $1 < z < 4$.

5.3 Star formation properties of the ALMA-detected sources

Determining the star-forming properties of faint SMGs is important in understanding the evolution of the cosmic SFRD because they are main contributors to the cosmic SFRD. We investigated the star formation mode of faint SMG counterparts to check whether or not their star-forming properties are similar to starburst galaxies.

Figure 5 plots the total SFRs ($\mathrm{SFR}_{\mathrm{UV}} + \mathrm{SFR}_{\mathrm{IR}}$) of SXDF-ALMA1, 2, 4, and 5 as functions of their stellar mass. We also show the average values of BzK galaxies derived by the PACS stacking analysis (Rodighiero et al. 2015), SMGs identified in ALESS surveys (Hodge et al. 2013) at $1.3 < z < 2.5$, and faint 1.3 mm sources detected with ALMA (Hatsukade et al. 2015). We plotted SFRs of the ALESS sources obtained by da Cunha et al. (2015) by fitting SEDs at ultraviolet to radio wavelengths. This figure shows that SXDF-ALMA1, 2, 4, and 5 are located in the main sequence. This means that they are more like "normal" star-forming galaxies rather than extreme starburst
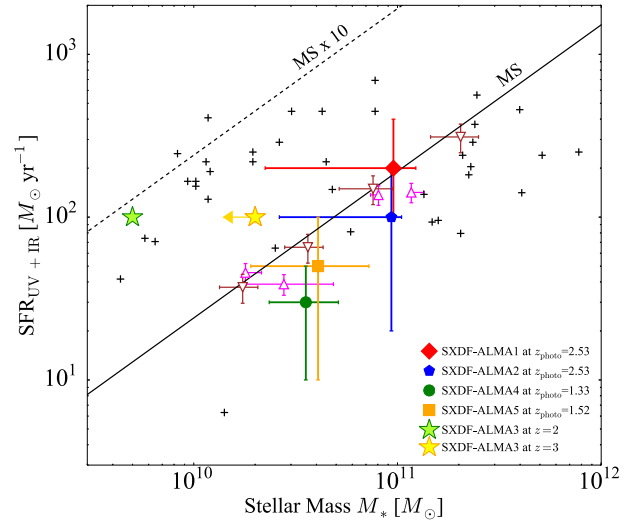

Fig. 5. SFRs derived from ultraviolet and infrared luminosities plotted against their stellar masses. The diamond, hexagon, circle, and square symbols represent SXDF-ALMA1, 2, 4, and 5, respectively. The solid line indicates the main sequence for star-forming galaxies at $1.4 < z < 2.5$ as defined by Daddi et al. (2007). The dashed line indicates the loci 10 times above the main sequence. The black crosses indicate ALESS sources at $1.3 < z < 2.5$ from da Cunha et al. (2015). The magenta triangles are faint 1.3 mm sources detected by ALMA (Hatsukade et al. 2015). Note that Hatsukade et al. (2015) used 68% confidence intervals, whereas we used 99% confidence intervals. The brown inverted triangles are the average values of BzK galaxies derived from the PACS stacking analysis (Rodighiero et al. 2015). The green and yellow stars indicate when SXDF-ALMA3 lay at $z = 2$ and when SXDF-ALMA3 lay at $z = 3$, respectively. Note that the stellar mass of SXDF-ALMA3 at $z = 3$ was at the 3σ upper limit because the rest-frame H-band was not detected.

galaxies. These results are consistent with those of Koprowski et al. (2014) and Hatsukade et al. (2015). Note that the total SFR of SXDF-ALMA1 should be treated as an upper limit because we used the 3σ upper limit value as its SFR_{UV}. However, this does not affect our results because the SFR_{UV} of SXDF-ALMA1 is negligible compared to its SFR_{IR} (see table 2).

Figure 5 also shows the constraints of the stellar mass and SFR of SXDF-ALMA3. The results imply that SXDF-ALMA3 is a starburst galaxy with a small stellar mass compared to bright SMGs ($M_* \sim 9.0 \times 10^{10} \, M_\odot$ using Chabrier IMF: Hainline et al. 2011). Submillimeter sources such as SXDF-ALMA3 have been missed in previous deep optical/near-infrared surveys and submillimeter single-dish surveys. Future spectroscopic identification of such sources with ALMA is highly encouraged.

Finally, we compared our results with the theoretical predictions obtained by recent simulations and semi-analytical models. Béthermin et al. (2012) empirically predicted the number counts at far-infrared and millimeter wavelengths from mid-infrared and radio number counts, and suggested that galaxies with $S_{1.1mm} \lesssim 1\,mJy$ are more likely to be associated with main sequence star-forming galaxies by using the SED library based on Herschel observations. From a theoretical point of view, Hayward et al. (2013) predicted the number counts at submillimeter wavelengths from a semi-empirical model with three-dimensional hydrodynamical simulations and three-dimensional dust radiative transfer, and also suggested that galaxies with $S_{1.1mm} < 1\,mJy$ are more likely to be associated with main sequence star-forming galaxies. These predictions are consistent with our results that two of the three faint SMGs (SXDF-ALMA4 and 5) are main sequence star-forming galaxies, as shown in figure 5.

6 Summary

We detected five submillimeter sources ($S_{1.1mm} = 0.54$–$2.02\,mJy$) in the SXDF-UDS-CANDELS field by using ALMA. The two brightest sources correspond to a known single-dish (AzTEC) selected bright SMG, whereas the remaining three are faint SMGs newly uncovered by ALMA. Our main results are as follows:

- If we exclude SXDF-ALMA1 and 2 to avoid the contribution of the known AzTEC source, the contribution of the faint SMGs to the infrared extragalactic background light is estimated to be $\sim 4.1^{+5.4}_{-3.0}\,Jy\,deg^{-2}$, which corresponds to $\sim 16^{+22}_{-12}\%$ of the infrared extragalactic background light. This suggests that their contribution to the infrared extragalactic background light is as large as that of bright SMGs ($S_{1.1mm} \geq 1.0\,mJy$, $\sim 2.9\,Jy\,deg^{-2}$; Hatsukade et al. 2011).

- The infrared SFRD of SXDF-ALMA3, 4, and 5 for $1 < z < 4$ is estimated to be $\sim (0.3$–$2) \times 10^{-2} \, M_\odot \, yr^{-1} \, Mpc^{-3}$. This value is as large as the contribution to infrared SFRD of bright SMGs at $z \simeq 2$–3.

- For four of the five ALMA sources (SXDF-ALMA1, 2, 4, and 5), we obtained the photometric redshifts and M_* by SED fitting at optical-to-near-infrared wavelengths: $z_{photo} \simeq 1.3$–2.5, $M_* \simeq (3.5$–$9.5) \times 10^{10} \, M_\odot$. The SFRs were estimated from ultraviolet and infrared luminosities as follows: $SFR_{UV+IR} \simeq 30$–$200 \, M_\odot \, yr^{-1}$. We also obtained their sSFRs ($\simeq 0.8$–$1\,Gyr^{-1}$). The derived values indicate that they are more like "normal" star-forming galaxies than starburst galaxies.

- SXDF-ALMA3 is faint in the optical-to-near-infrared ($H = 25.30 \pm 0.25$), despite its infrared luminosity ($L_{IR} \simeq 1 \times 10^{12} \, L_\odot$ or $SFR \simeq 100 \, M_\odot \, yr^{-1}$). The optical-to-radio SED suggests that this object is located at $z \simeq 2$–3. The inferred stellar mass ($M_* \sim 5 \times 10^9$ or $< 2 \times 10^{10}$ at $z = 2$ or $z = 3$, respectively) was likely to be smaller than those of the other ALMA sources. These results suggest that this object may be a starburst galaxy with a small stellar mass at $z \simeq 2$–3. The contribution of SXDF-ALMA3 to the cosmic SFRD may be $\sim 1\%$–10% of the infrared SFRD.

Appendix. Estimation of infrared luminosities

As described in subsection 4.2, we used the SED templates obtained by Dale and Helou (2002) to estimate infrared luminosities of the ALMA sources. Figure 6 plots the SED
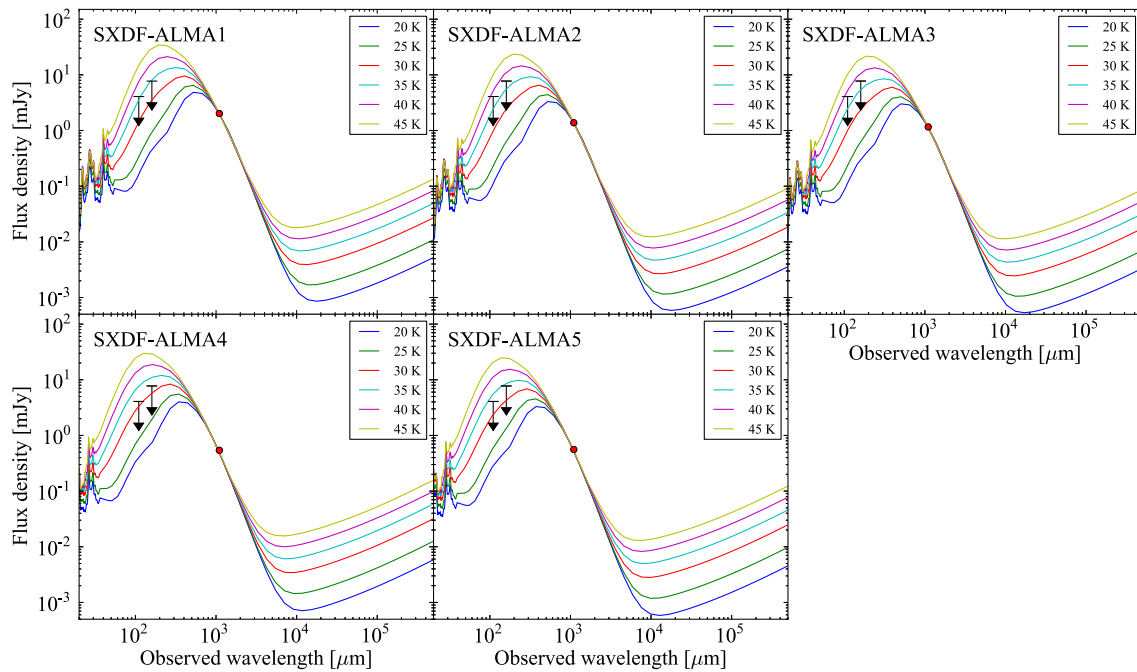
Fig. 6. SED templates by Dale and Helou (2002) scaled to the observed flux densities at 1.1 mm ($S_{1.1mm total}$). The blue, green, red, cyan, magenta, and yellow solid lines indicate SED templates with T_{dust} = 20, 25, 30, 35, 40, and 45 K, respectively. The red circles are the observed flux densities at 1.1 mm. The black arrows represent the 3σ upper limits on Herschel/PACS 100 μm and 160 μm.

templates scaled to the observed flux densities at 1.1 mm ($S_{1.1mm total}$). Here, we show the SED templates with T_{dust} = 20, 25, 30, 35, 40, and 45 K. The ALMA sources were not detected at Herschel/PACS 100 μm and 160 μm. As shown in the figure, the 3σ upper limits on Herschel/PACS photometry could place a stringent constraint on T_{dust}. The upper limits on the Herschel/PACS photometry are clearly below the SED templates with T_{dust} = 40 and 45 K. For SXDF-ALMA4, they are clearly below the SED templates with T_{dust} = 35, 40, and 45 K. Therefore, we assumed T_{dust} = 20–35 K (T_{dust} = 20–30 K for SXDF-ALMA4) to estimate the infrared luminosities of ALMA sources.

For each ALMA source, we integrated SED templates with T_{dust} = 20, 25, 30, and 35 K (T_{dust} = 20, 25, and 30 K for SXDF-ALMA4) between the rest-frames 8 and 1000 μm and adopted the average, minimum, and maximum values as the infrared luminosity, lower limit of the infrared luminosity, and upper limit of the infrared luminosity, respectively.

References

Alexander, D. M., Bauer, F. E., Chapman, S. C., Smail, I., Blain, A. W., Brandt, W. N., & Ivison, R. J. 2005, ApJ, 632, 736

Armus, L., et al. 2007, ApJ, 656, 148

Ashby, M. L. N., et al. 2013, ApJ, 769, 80

Barger, A. J., Cowie, L. L., Sanders, D. B., Fulton, E., Taniguchi, Y., Sato, Y., Kawara, K., & Okuda, H. 1998, Nature, 394, 248

Béthermin, M., et al. 2012, ApJ, 757, L23

Blain, A. W., Smail, I., Ivison, R. J., Kneib, J.-P., & Frayer, D. T. 2002, Phys. Rep., 369, 111

Bolzonella, M., Miralles, J.-M., & Pelló, R. 2000, A&A, 363, 476

Brammer, G. B., van Dokkum, P. G., & Coppi, P. 2008, ApJ, 686, 1503

Bruzual A., G., & Charlot, S. 1993, ApJ, 405, 538

Bruzual, G., & Charlot, S. 2003, MNRAS, 344, 1000 (BC03)

Burgarella, D., et al. 2013, A&A, 554, A70

Calzetti, D., Armus, L., Bohlin, R. C., Kinney, A. L., Koornneef, J., & Storchi-Bergmann, T. 2000, ApJ, 533, 682

Caputi, K. I., Cirasuolo, M., Dunlop, J. S., McLure, R. J., Farrah, D., & Almaini, O. 2011, MNRAS, 413, 162

Carniani, S., et al. 2015, A&A, 584, A78

Casey, C. M., et al. 2013, MNRAS, 436, 1919

Chabrier, G. 2003, PASP, 115, 763

Chapman, S. C., et al. 2010, MNRAS, 409, L13

Chapman, S. C., Blain, A. W., Smail, I., & Ivison, R. J. 2005, ApJ, 622, 772

Chen, C.-C., Cowie, L. L., Barger, A. J., Wang, W.-H., & Williams, J. P. 2014, ApJ, 789, 12

Coppin, K., et al. 2006, MNRAS, 372, 1621

da Cunha, E., et al. 2015, ApJ, 806, 110

Daddi, E., et al. 2007, ApJ, 670, 156

Dale, D. A., & Helou, G. 2002, ApJ, 576, 159

Dunlop, J. S., et al. 2016, arXiv:1606.00227

Eales, S., Lilly, S., Gear, W., Dunne, L., Bond, J. R., Hammer, F., Le Fèvre, O., & Crampton, D. 1999, ApJ, 515, 518

Elbaz, D., et al. 2011, A&A, 533, A119

Ezawa, H., Kawabe, R., Kohno, K., & Yamamoto, S. 2004, Proc. SPIE, 5489, 763

Fazio, G. G., et al. 2004, ApJS, 154, 10

Fixsen, D. J., Dwek, E., Mather, J. C., Bennett, C. L., & Shafer, R. A. 1998, ApJ, 508, 123

Fontana, A., et al. 2014, A&A, 570, A11

Ford, H. C., et al. 1998, SPIE, 3356, 234

Fujimoto, S., Ouchi, M., Ono, Y., Shibuya, T., Ishigaki, M., Nagai, H., & Momose, R. 2016, ApJS, 222, 1

Furusawa, H., et al. 2008, ApJS, 176, 1

Galametz, A., et al. 2013, ApJS, 206, 10

Gehrels, N. 1986, ApJ, 303, 336

Goto, T., et al. 2011, MNRAS, 414, 1903

Greve, T. R., et al. 2010, ApJ, 719, 483

Greve, T. R., Ivison, R. J., Bertoldi, F., Stevens, J. A., Dunlop, J. S., Lutz, D., & Carilli, C. L. 2004, MNRAS, 354, 779

Griffin, M. J., et al. 2010, A&A, 518, L3

Grogin, N. A., et al. 2011, ApJS, 197, 35

Hainline, L. J., Blain, A. W., Smail, I., Alexander, D. M., Armus, L., Chapman, S. C., & Ivison, R. J. 2011, ApJ, 740, 96

Hatsukade, B., et al. 2011, MNRAS, 411, 102

Hatsukade, B., et al. 2016, PASJ, 68, 36

Hatsukade, B., Ohta, K., Seko, A., Yabe, K., & Akiyama, M. 2013, ApJ, 769, L27

Hatsukade, B., Ohta, K., Yabe, K., Seko, A., Makiya, R., & Akiyama, M. 2015, ApJ, 810, 91

Hayward, C. C., Narayanan, D., Kereš, D., Jonsson, P., Hopkins, P. F., Cox, T. J., & Hernquist, L. 2013, MNRAS, 428, 2529

Hodge, J. A., et al. 2013, ApJ, 768, 91

Högbom, J. A. 1974, A&AS, 15, 417

Hughes, D. H., et al. 1998, Nature, 394, 241

Ilbert, O., et al. 2015, A&A, 579, A2

Kennicutt, R. C., Jr. 1998, ApJ, 498, 541

Kimble, R. A., MacKenty, J. W., O'Connell, R. W., & Townsend, J. A. 2008, Proc. SPIE, 7010, 70101E

Klaas, U., Haas, M., Heinrichsen, I., & Schulz, B. 1997, A&A, 325, L21

Knudsen, K. K., van der Werf, P. P., & Kneib, J.-P. 2008, MNRAS, 384, 1611

Koekemoer, A. M., et al. 2011, ApJS, 197, 36

Kohno, K., et al. 2016, arXiv:1601.00195

Koprowski, M. P., Dunlop, J. S., Michałowski, M. J., Cirasuolo, M., & Bowler, R. A. A. 2014, MNRAS, 444, 117

Kriek, M., van Dokkum, P. G., Labbé, I., Franx, M., Illingworth, G. D., Marchesini, D., & Quadri, R. F. 2009, ApJ, 700, 221

Laird, E. S., Nandra, K., Pope, A., & Scott, D. 2010, MNRAS, 401, 2763

Lawrence, A., et al. 2007, MNRAS, 379, 1599

Magdis, G. E., et al. 2011, A&A, 534, A15

Magnelli, B., et al. 2014, A&A, 561, A86

McMullin, J. P., Waters, B., Schiebel, D., Young, W., & Golap, K. 2007, in ASP Conf. Ser., 376, Astronomical Data Analysis Software and Systems XVI, ed. R. A. Shaw et al. (San Francisco: ASP), 127

Mentuch Cooper, E., et al. 2012, ApJ, 755, 165

Michałowski, M. J., Dunlop, J. S., Cirasuolo, M., Hjorth, J., Hayward, C. C., & Watson, D. 2012, A&A, 541, A85

Michałowski, M. J., Hayward, C. C., Dunlop, J. S., Bruce, V. A., Cirasuolo, M., Cullen, F., & Hernquist, L. 2014, A&A, 571, A75

Miyazaki, S., et al. 2002, PASJ, 54, 833

Moran, J. M. 1998, Proc. SPIE, 3357, 208

Nguyen, H. T., et al. 2010, A&A, 518, L5

Oliver, S. J., et al. 2012, MNRAS, 424, 1614

Ono, Y., et al. 2010, MNRAS, 402, 1580

Ono, Y., Ouchi, M., Kurono, Y., & Momose, R. 2014, ApJ, 795, 5

Oteo, I., Zwaan, M. A., Ivison, R. J., Smail, I., & Biggs, A. D. 2016, ApJ, 822, 36

Ott, S. 2010, in ASP Conf. Ser., 434, Astronomical Data Analysis Software and Systems XIX, ed. Y. Mizumoto et al. (San Francisco: ASP), 139

Ouchi, M., et al. 2004, ApJ, 611, 660

Oyaizu, H., Lima, M., Cunha, C. E., Lin, H., & Frieman, J. 2008, ApJ, 689, 709

Pereira-Santaella, M., Alonso-Herrero, A., Rieke, G. H., Colina, L., Díaz-Santos, T., Smith, J.-D. T., Pérez-González, P. G., & Engelbracht, C. W. 2010, ApJS, 188, 447

Poglitsch, A., et al. 2010, A&A, 518, L2

Pope, A., et al. 2008, ApJ, 675, 1171

Puget, J.-L., Abergel, A., Bernard, J.-P., Boulanger, F., Burton, W. B., Desert, F.-X., & Hartmann, D. 1996, A&A, 308, L5

Rieke, G. H., et al. 2004, ApJS, 154, 25

Robertson, B. E., Ellis, R. S., Dunlop, J. S., McLure, R. J., Stark, D. P., & McLeod, D. 2014, ApJ, 796, L27

Rodighiero, G., et al. 2011, ApJ, 739, L40

Rodighiero, G., et al. 2014, MNRAS, 443, 19

Rodighiero, G., et al. 2015, ApJ, 800, L10

Schreiber, C., et al. 2015, A&A, 575, A74

Scott, K. S., et al. 2010, MNRAS, 405, 2260

Scott, K. S., et al. 2012, MNRAS, 423, 575

Silva, L., Granato, G. L., Bressan, A., & Danese, L. 1998, ApJ, 509, 103

Simpson, J. M., et al. 2014, ApJ, 788, 125

Skelton, R. E., et al. 2014, ApJS, 214, 24

Smail, I., Ivison, R. J., & Blain, A. W. 1997, ApJ, 490, L5

Smolčić, V., et al. 2012, A&A, 548, A4

Swinbank, A. M., et al. 2014, MNRAS, 438, 1267

Symeonidis, M., et al. 2013, MNRAS, 431, 2317

Tadaki, K.-i., et al. 2015, ApJ, 811, L3

Tadaki, K.-i., Kodama, T., Tanaka, I., Hayashi, M., Koyama, Y., & Shimakawa, R. 2013, ApJ, 778, 114

Takagi, T., Ono, Y., Shimasaku, K., & Hanami, H. 2008, MNRAS, 389, 775

Takeuchi, T. T., Buat, V., & Burgarella, D. 2005, A&A, 440, L17

Tody, D. 1993, in ASP Conf. Ser., 52, Astronomical Data Analysis Software and Systems II, ed. R. J. Hanisch et al. (San Francisco: ASP), 173

Ueda, Y., et al. 2008, ApJS, 179, 124

Umehata, H., et al. 2014, MNRAS, 440, 3462

van Moorsel, G., Kemball, A., & Greisen, E. 1996, in ASP Conf. Ser., 101, Astronomical Data Analysis Software and Systems V, ed. G. H. Jacoby & J. Barnes (San Francisco: ASP), 37

Wang, W.-H., Cowie, L. L., van Saders, J., Barger, A. J., & Williams, J. P. 2007, ApJ, 670, L89

Wardlow, J. L., et al. 2011, MNRAS, 415, 1479

Weiß, A., et al. 2009, ApJ, 707, 1201

Wilson, G. W., et al. 2008, MNRAS, 386, 807

Wuyts, S., et al. 2011, ApJ, 738, 106

Yagi, M., Kashikawa, N., Sekiguchi, M., Doi, M., Yasuda, N., Shimasaku, K., & Okamura, S. 2002, AJ, 123, 66